Cellulose
https://doi.org/10.1007/s10570-026-07089-x

ORIGINAL RESEARCH

A templating approach for porous silica bioactive glass using sodium methylcellulose

Maryam Sarmast Shoushtari · Dayang Radiah Awang Biak · D. A. Hoey · N. Abdullah · H. S. Zainuddin · S. Kamarudin

Received: 27 January 2025 / Accepted: 17 May 2026

Abstract This study presents a templating strategy using sodium carboxymethylcellulose (CMC), a biodegradable and biocompatible polysaccharide, to synthesize porous SiO_2–CaO–P_2O_5–Na_2O bioactive glass via the sol–gel method. CMC was selected because its hydrophilic and film-forming properties facilitate homogeneous gelation, and its complete thermal decomposition during calcination leaves interconnected pores that enhance scaffold bioactivity. Two formulations, CMC5 and CMC10, were prepared by incorporating 5 wt.% and 10 wt.% CMC into the sol, enabling evaluation of template concentration on structure and performance. Characterization revealed that CMC templating increased porosity and pore volume without altering the glass chemistry, while XRD confirmed changes in crystallinity with higher CMC content. Mechanically, CMC5 achieved improved compressive strength (3.6 MPa) and modulus (2.1 MPa) compared to pure BG, aligning with cancellous bone requirements. In vitro tests demonstrated enhanced hydroxyapatite formation in simulated body fluid and high cell viability in MC3T3 cultures, particularly for CMC5. These findings highlight CMC templating as a simple and effective approach to tune porosity and performance of sol–gel bioactive glass for bone tissue engineering applications.

Supplementary Information The online version contains supplementary material available at https://doi.org/10.1007/s10570-026-07089-x.

M. S. Shoushtari · D. R. Awang Biak (✉) · N. Abdullah · H. S. Zainuddin · S. Kamarudin
Department of Chemical and Environmental Engineering, Faculty of Engineering, Universiti Putra Malaysia, Serdang, Selangor, Malaysia
e-mail: dradiah@upm.edu.my

D. R. Awang Biak
Institute of Nanomaterial and Nanotechnology, Universiti Putra Malaysia, Serdang, Selangor, Malaysia

D. A. Hoey
Trinity Centre for Biomedical Engineering, Trinity Biomedical Sciences Institute, Trinity College Dublin, Dublin, Ireland

D. A. Hoey
Department of Mechanical, Manufacturing, and Biomedical Engineering, School of Engineering, Trinity College, Dublin, Ireland

D. A. Hoey
Advanced Materials and Bioengineering Research Centre, Trinity College Dublin & RCSI, Dublin, Ireland

Published online: 11 July 2026

Graphical abstract

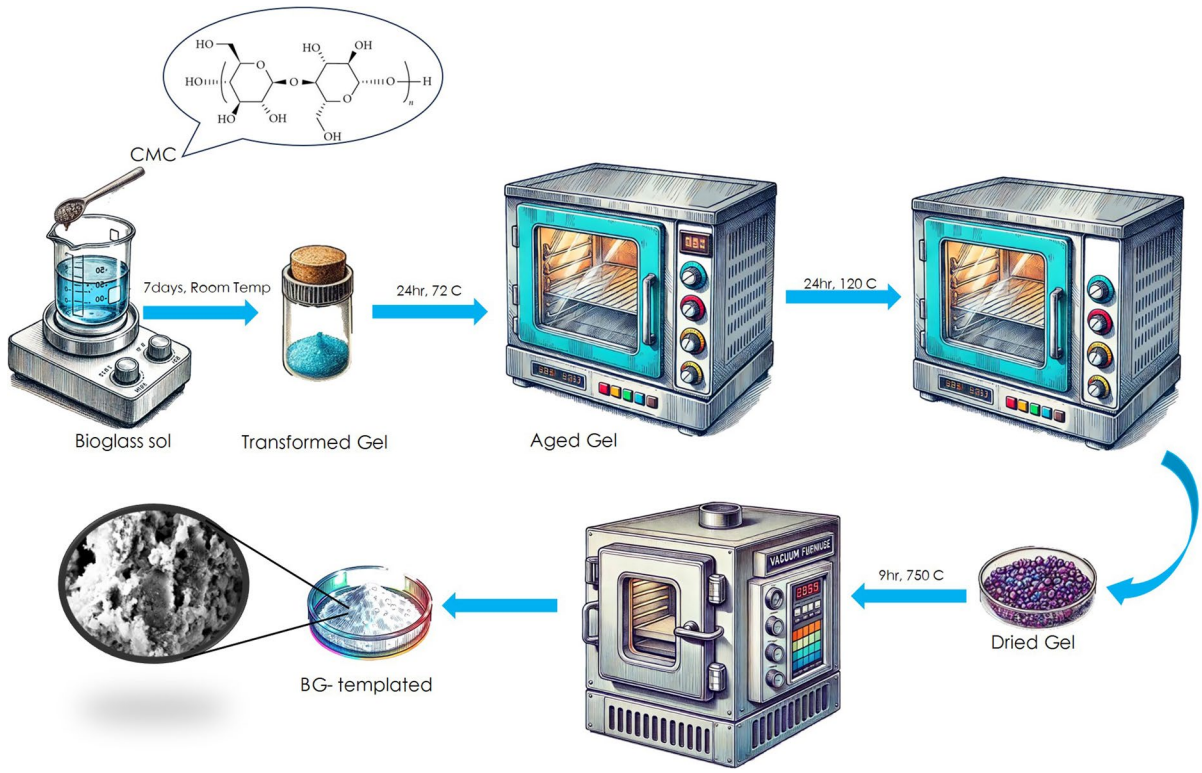

Keywords Bioglass · Sol–gel · Sodium methylcellulose · Template

Introduction

Bioactive glasses (BGs) are widely studied for bone tissue engineering because of their ability to bond with bone and stimulate cellular responses (Jones 2015). Their performance is strongly influenced by porosity and surface area, which enhance ion exchange and support cell proliferation. However, achieving interconnected three-dimensional pore structures while retaining sufficient strength remains a challenge, as increased porosity often reduces mechanical stability and can cause stress-shielding effects (Dutta et al. 2017). To overcome these limitations, templating methods have been developed to introduce controlled porosity. Sacrificial templates such as bacterial cellulose, cellulose nanofiber, PEG, rice husk, and sugarcane bagasse have been used to create porous BG scaffolds with improved interconnectivity (Gupta et al. 2015; Hu et al. 2022; Lei et al. 2012; Luo et al. 2016; Qian et al. 2009; Sarmast Sh et al. 2022; Wu et al. 2009). While effective, these approaches often suffer from poor reproducibility or limited control over pore morphology. Thus, there remains a need for simple, low-cost, and reliable templating strategies.

Sodium carboxymethylcellulose (CMC) is a hydrophilic macromolecule with significant potential for various medical and pharmaceutical applications. CMC synthesis involves cellulose's swelling with sodium hydroxide, followed by an alkali-catalyzed reaction with chloroacetic acid (Sudhakar et al. 2006; Babaluei et al. 2023; Rimpy and Ahuja 2022). It is used in tissue regeneration because of its outstanding properties, including biodegradability, non-toxicity, biocompatibility, film-forming capabilities, and pH sensitivity (Babaluei et al. 2023; Hu et al. 2018). Recent studies have demonstrated various applications and impacts of CMC in sol–gel processes. CMC

plays a crucial role in sol–gel systems by mediating polymer interactions, phase separation, and electrostatic balance. For example, its incorporation with protonated polyethyleneimine via CO_2 leads to polyelectrolyte complex gels with controlled structural organization (Huang et al. 2024). In spray-dried silica systems, CMC combined with surfactants acts as a structure-directing agent that governs crystallization and phase formation (Albar et al. 2023). Likewise, in ZnO/SiO_2 sol–gel spray drying, CMC actively tailors particle morphology and surface chemistry, thereby influencing photoluminescence and crystallization behavior (Ajiz et al. 2023).

Despite these advantages, systematic evaluation of CMC templating on sol–gel templated BG remains limited. In this study, we investigate the effect of adding sodium CMC at two concentrations (5% and 10% w/v) on the morphology, porosity, crystallinity, mechanical strength, in-vitro bioactivity, antibacterial activity, and cell viability of SiO_2–CaO–P_2O_5–Na_2O BG. By elucidating the role of CMC in modulating both structural integrity and biological response, this study establishes a simple and effective strategy to enhance the performance of sol–gel-derived bioactive glass scaffolds for cancellous bone applications.

Materials and methods

Materials

Tetraethyl orthosilicate (TEOS, $Si(OC_2H_5)_4$, 98%), triethyl phosphate (TEP, $C_6H_{15}O_4P$, 99%), calcium nitrate tetrahydrate ($Ca(NO_3)_2{\cdot}4H_2O$, 99%), and sodium nitrate ($NaNO_3$, 99%) were purchased from Merck (Germany). Sodium carboxymethylcellulose (CMC, degree of substitution 0.7, MW ~ 90,000 g/mol) was obtained from Aprin Advanced Technologies Development (Tehran, Iran) and used as a sacrificial template. All reagents were of analytical grade and used without further purification.

Synthesis of bioactive glass (BG) and CMC-templated BG

The SiO_2–CaO–P_2O_5–Na_2O glass (BG) was synthesized by a sol–gel route (nominal molar composition: $60SiO_2$–$30CaO$–$6P_2O_5$–$4Na_2O$, mol%). TEOS was hydrolyzed in ethanol and deionized water with HNO_3 as a catalyst (pH ~ 2). TEP was then added dropwise, followed by $Ca(NO_3)_2{\cdot}4H_2O$ and $NaNO_3$ under continuous stirring for 1 h. The solution was allowed to gel at room temperature and aged for 72 h. Drying was carried out at 60 °C for 24 h. The process is illustrated in Fig. 1.

The carboxymethyl cellulose (CMC) used in this study was obtained in powder form (Aprin Advanced Technologies Development, Tehran, Iran) and employed as a sacrificial template. Samples were designated as CMC5 and CMC10, where the number indicates the weight percentage (wt.%) of CMC added to the bioactive glass sol (5 wt.% and 10 wt.%). For synthesis, the desired amount of CMC powder was directly dispersed into the freshly prepared BG sol and stirred for 1 h to obtain a homogeneous BG–CMC sol. After gelation and drying, the samples were calcined at 750 °C for 9 h. During this process, the incorporated CMC underwent complete thermal decomposition, resulting in the formation of interconnected pores within the glass matrix. This templating effect of CMC was utilized to control the porosity and microstructure of the scaffolds. The aging and sintering conditions were maintained identical to those applied to the pure BG samples.

Characterization

Functional groups were analyzed by FTIR spectroscopy (Spectrum 100, Perkin Elmer) over 4000–500 cm^{-1} with a resolution of 2 cm^{-1} (120 scans). Samples were mixed with KBr (300 mg) and pressed into pellets. Peaks were identified in both the functional group and fingerprint regions.

The morphology was examined using a Scanning Electron Microscope (S-3400N, Thermo Scientific, USA). The scan was performed at an accelerating voltage of 20 kV. Prior to imaging, all samples were sputter-coated with a thin conductive layer of gold (Au) to prevent charging effects. SEM micrographs were acquired at a magnification of 1000×, while inset images were recorded at 5000× to highlight finer surface features. In conjunction with SEM imaging, Energy Dispersive X-Ray (EDX) analysis (Oxford Instruments, Max 20, UK) was carried out to determine the elemental composition of the samples, namely the Si, Ca, P, Na, and O.

Crystalline phases were analyzed using an X-ray Diffractometer (X'Pert Pro PANalytical, PW 3040/60,

Fig. 1 Graphical abstract

Netherlands) equipped with a Cu radiation source operated at 40 kV and 40 mA over the 2θ range of 20–70°. A Ni filter was used to suppress Cu Kβ radiation. Therefore, the diffraction patterns contained the Cu Kα doublet ($K\alpha_1/K\alpha_2$) with an effective wavelength of 1.5418 Å.

Prior to phase identification, background correction was applied to reduce diffuse scattering contributions and improve peak visualization. The diffraction peaks were indexed according to the standard PDF database, and the major crystalline reflections were assigned to sodium calcium silicate ($Na_2Ca_2Si_3O_9$, combeite phase).

The crystallite size was determined by the Scherrer (1918) Eq. (1), where K = 0.9, λ = 0.15418 nm, β is the full width at half maximum (FWHM) in radians, and the Bragg angle θ must be supplied in accordance with the method of determining its cosine value.

$$Crystallite\ Size = \frac{K\lambda}{\beta \mathrm{Cos}\theta}. \tag{1}$$

Crystallinity (%) was estimated from the ratio of the integrated crystalline peak area (A_c) to the total dfracted area ($A_c + A_a$) after baseline correction (Eq. 2):

$$\%\mathrm{Crystallinity} = \frac{Ac}{Ac + Aa} \times 100 \tag{2}$$

where A_c represents the crystalline peak area and A_a corresponds to the amorphous halo contribution.

Porosity and apparent density of the BG samples, before and after templating, were measured using the ethanol displacement method described by Guan et al. (2005). The initial sample weight (W_i) was recorded, then the sample was immersed in a known volume of ethanol (V_1) for 15 min to fill the pores. The combined volume of ethanol and sample (V_2) and the remaining ethanol volume after removal (V_3) were measured. Porosity and density were calculated as described by Wang et al. (2016):

$$\%\mathrm{Porosity} = \frac{V1 - V3}{V2 - V3} \times 100 \tag{3}$$

$$\mathrm{Density} = \frac{Wi}{V2 - V1} \tag{4}$$

Pore volume, specific surface area, and average pore size of the BG samples were determined via BET analysis (Quantachrome, Autosorb-1, USA). Porosity before and after templating was estimated

using nitrogen adsorption/desorption processes. The samples underwent two-stage degassing processes to remove moisture, *i.e*. first at 90 °C for 60 min, then at 250 °C for 540 min, both at 10 °C/min. Measurements were performed under vacuum in a nitrogen environment at 77 K.

The swelling experiment involved submerging the disc-shaped samples of BG in distilled water. The disc-shaped sample was placed in a polyethylene bottle containing 25 ml of distilled water and placed in an incubator at 37 °C for a week without agitation. At regular intervals, the disc was taken out of the container, and any excess water was gently removed by wiping the surface with tissue paper. The extent of swelling, or changes in the shape of the disc sample, was measured. Equation (5) was used to determine the water intake, where M_i represents the initial mass of the sample, and M_f represents the final weight of the sample.

$$\Delta W\% = \frac{Mf - Mi}{Mi} \times 100 \tag{5}$$

Cylindrical specimens for mechanical testing were prepared by wet pressing the BG powders into cylindrical molds (5.0 ± 0.5 mm diameter and 10 ± 0.5 mm height), followed by drying at 40 °C to obtain dense sample. The compressive mechanical properties were then measured according to ASTM D638 (Type V) using a universal testing machine (Instron 3365, Instron, America) equipped with a 50 N load cell at a crosshead speed of 5 mm/min.

Bioactivity was assessed by monitoring apatite formation on BG surfaces in simulated body fluid (SBF) prepared according to Kokubo and Takadama (2006) and ISO 23317–2007. Samples were incubated at 37 °C in 32 mL of SBF for 1, 7, 14, 21, and 28 days. Two different treatments were applied to each sample:

"NR" (non-refreshment): No SBF solution was replaced or adjusted throughout the experiment.

"R" (refreshment): SBF solutions were refreshed every 24 h to maintain a pH of 7.42.

After incubation, samples were rinsed, dried, and analyzed for presence of hydroxyapatite using SEM (S-3400N, Thermo Scientific, USA) and XRD (X'Pert Pro PANalytical, Netherlands). Ion release (e.g., Ca) was quantified via ICP-OES (PerkinElmer® Optima 7300 DV, USA) using fresh SBF as a control.

In-vitro degradation study of the BGs was performed in PBS solution at pH 7.4 and 37 °C for a week. Initially, the weight of each specimen was measured. Then, the samples were carefully removed from the media, washed with distilled water, and dried in a desiccator for 24 h at room temperature. M_i and M_f denoted the initial and final weight of the dried samples at each sampling time, respectively. Equation (7) was used to calculate the degradation:

$$\text{Degradation}\% = \frac{Mi - Mf}{Mi} \times 100 \tag{6}$$

The disk shape specimens with a diameter of 10 ± 2 mm and height of 2 ± 1 mm were prepared as recommended in ISO 23317–2007 for bioactivity and biodegradation measurement.

In-vitro antibacterial activity of BG samples was tested against *S. aureus* (ATCC® 6538, Gram-positive) and *E. coli* (ATCC® 8739, Gram-negative). Bacteria were cultured in NB or LB broth, serially diluted to ~ 10^8 CFU/mL, and 10 mg of UV-sterilized samples were incubated with 1 mL of bacterial suspension at 37 °C and 150 rpm for 18 h. Optical density at 600 nm (ODs) was measured, and bacterial inhibition (%) was calculated as:

$$\text{Bacterial inhibition}\% = \frac{ODc - ODs}{ODc} \times 100 \tag{7}$$

Cell viability was evaluated using an MTT assay with MC3T3 mouse embryonic fibroblasts (Ciapetti et al. 1993; Mukundan et al. 2013; Rezaeipour et al. 2023). Approximately 7×10^3 cells were seeded per well in 96-well plates and incubated for 24 h to allow attachment. The culture medium was then replaced with 100 µL of sample extracts prepared by incubating 0.1 g of BG or BG–CMC in DMEM at 37 °C overnight, diluted to 25%, 50%, and 100%. After 24 h incubation at 37 °C with 5% CO_2, 10 µL of MTT solution (5 mg/mL in PBS) was added to each well to achieve a final concentration of 0.5 mg/mL, followed by 3 h incubation. The medium was removed, and 100 µL of DMSO was added to dissolve the formazan crystals. Absorbance was measured at 570 nm using a microplate reader, and cell viability

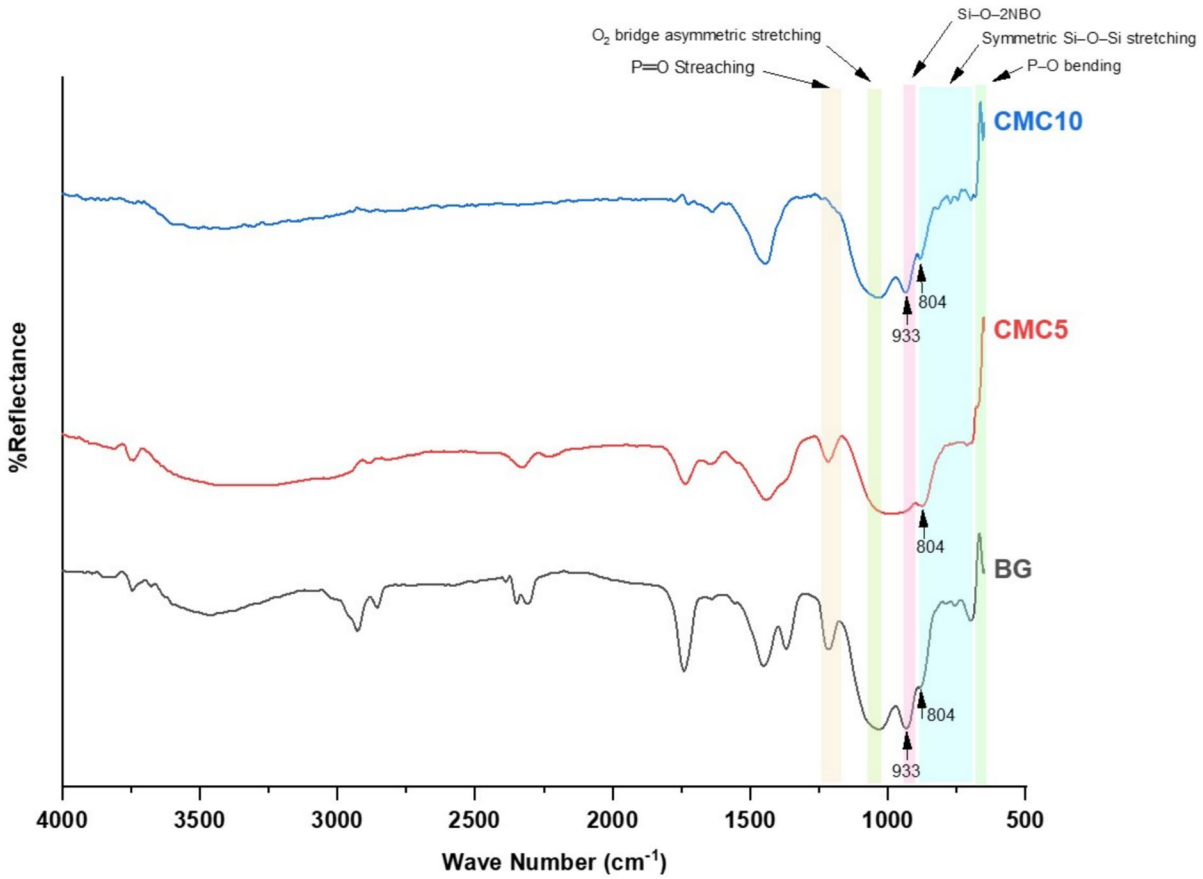

Fig. 2 FTIR spectra of pure BG and BG-CMC

(%) was calculated relative to the untreated control after blank correction:

$$\text{Cell Viability}\% = \frac{Absorbance\ sample(mean)}{Absorbance\ control(mean)} \times 100 \quad (8)$$

The data were analyzed using one-way ANOVA with Holm-Bonferroni post-hoc analysis. The values presented are means ± standard deviation for three independent replicates, and statistical significance was denoted as $*P \leq 0.05$, $**P \leq 0.01$, and $***P \leq 0.001$.

Results and discussion

Fourier transform infrared (FTIR) spectroscopy.

The FTIR spectra of BG, CMC5, and CMC10 confirmed the characteristic of silicate and phosphate bands typical of sol–gel BG (Fig. 2, Table 1) (Haghighi et al. 2021; Sarmast Sh et al. 2023). The broad absorption band in the range of 3000–3500 cm^{-1} corresponds to O–H stretching vibrations. This peak originates from surface hydroxyl groups (≡Si–OH) and adsorbed water molecules remaining after sol–gel synthesis, as commonly reported for sol–gel-derived bioglasses (Zeitler and Cormack 2006; Dubey et al. 2021). The slight shift of the band toward ~ 3000 cm^{-1} is attributed to strong hydrogen bond between hydroxyl groups, resulting in band broadening. These surface silanol groups are important, as they serve as nucleation sites for hydroxyapatite formation during immersion in simulated body fluid (Kokubo and Takadama 2006; Gupta and Santhiya 2017).

Morphology analysis

The SEM–EDX analysis provided insights into the microstructure and elemental composition of BG

Table 1 FTIR characteristic bands of the synthesized BG

Band number (cm^{-1})	Vibration mode	References
600–610	P–O bending vibrations in PO_4^{3-} groups	Sarmast Sh et al. (2023)
703–703	**Symmetric Si–O–Si streching vibrations	Haghighi et al. (2021)
805–804	Attributed to BO (bridging Oxygen)	Haghighi et al. (2021)
930	**Symmetric Si–O–Si streching vibrations	Haghighi et al. (2021)
933	*Si–O–2NBO (non-bridging oxygen) stretching vibrations	Sarmast Sh et al. (2022)
1085–1061	Asymmetric stretching of bridging oxygen	Haghighi et al. (2021)
1210–1216	P═O Stretching vibrations	Sarmast Sh et al. (2023)

*This vibrational mode is associated with the presence of Ca^{2+} and Na^{+} among the tetrahedron glass network

**These Vibrational modes are assigned to the symmetric Si–O–Si stretching vibration in crystalline silicate SiO_4^{4-}

and BG-CMC. The pure BG sample displayed a uniform, dense, flaky and compact morphology. In contrast, the addition of 5 wt.% CMC resulted in a more uniform distribution of smaller particles and a refined porous structure (Fig. 3b). The SEM image of CMC10 showed larger, more spherical particles and smoother surfaces, indicating the templating effect of CMC (Fig. 3c).

Variations in surface morphology and porosity are closely associated with the influence of CMC on the sol–gel process and gelation behavior of the BG matrix. As a water-soluble polymer, CMC forms a gel-like network in solution and interacts with Ca^{2+} ions and bicarbonate species during sol formation, affecting the organization of the developing gel. The incorporation of 5% CMC likely enhanced these interactions, promoting greater pore interconnectivity and overall porosity. In contrast, lower CMC contents produced smaller pore diameters and a more compact network, consistent with the microstructural observations (Bi et al. 2020; Silva et al. 2021). During methylcellulose hydrolysis with HNO_3, the preferential attack on amorphous regions and expansion of crystalline domains may have induced structural rearrangement within the cellulose matrix (Silva et al. 2021), further influencing pore evolution. At higher CMC concentrations, its pronounced thickening effect led to a denser gel and smoother surface, as observed in the CMC10 sample. Such structural differences are expected to influence subsequent ion exchange, apatite nucleation, and mechanical integrity, highlighting the critical role of CMC content in tuning the microstructure and performance of sol–gel-derived bioglass scaffolds.

The EDX analysis confirmed the presence of key components such as silica (Si), sodium (Na), and calcium (Ca) in all samples. The detected amount of SiO_2 in BG, CMC5, and CMC10 was 40.9%, 42.15%, and 41.51%, respectively. These slight deviations in the elemental composition compared to the elements in 45S5 Bioglass® suggest that incorporating CMC does not significantly alter the elemental composition but rather improves the structural properties of the bioglass.

Porosity and density analyses

Porosity is a critical parameter in scaffold design, governing cell attachment, nutrient diffusion, and vascularization. As shown in Fig. 4, the porosity values were approximately 52.5% for BG, 60% for CMC5, and 58% for CMC10, with corresponding apparent densities ranging from 0.86 g/cm^3 (BG) to 0.93–0.96 g/cm^3 for the BG-CMC samples. Although the BG–CMC samples exhibited higher average porosity and density values than pristine BG, the relatively large standard deviations indicate substantial variability between samples. Therefore, these

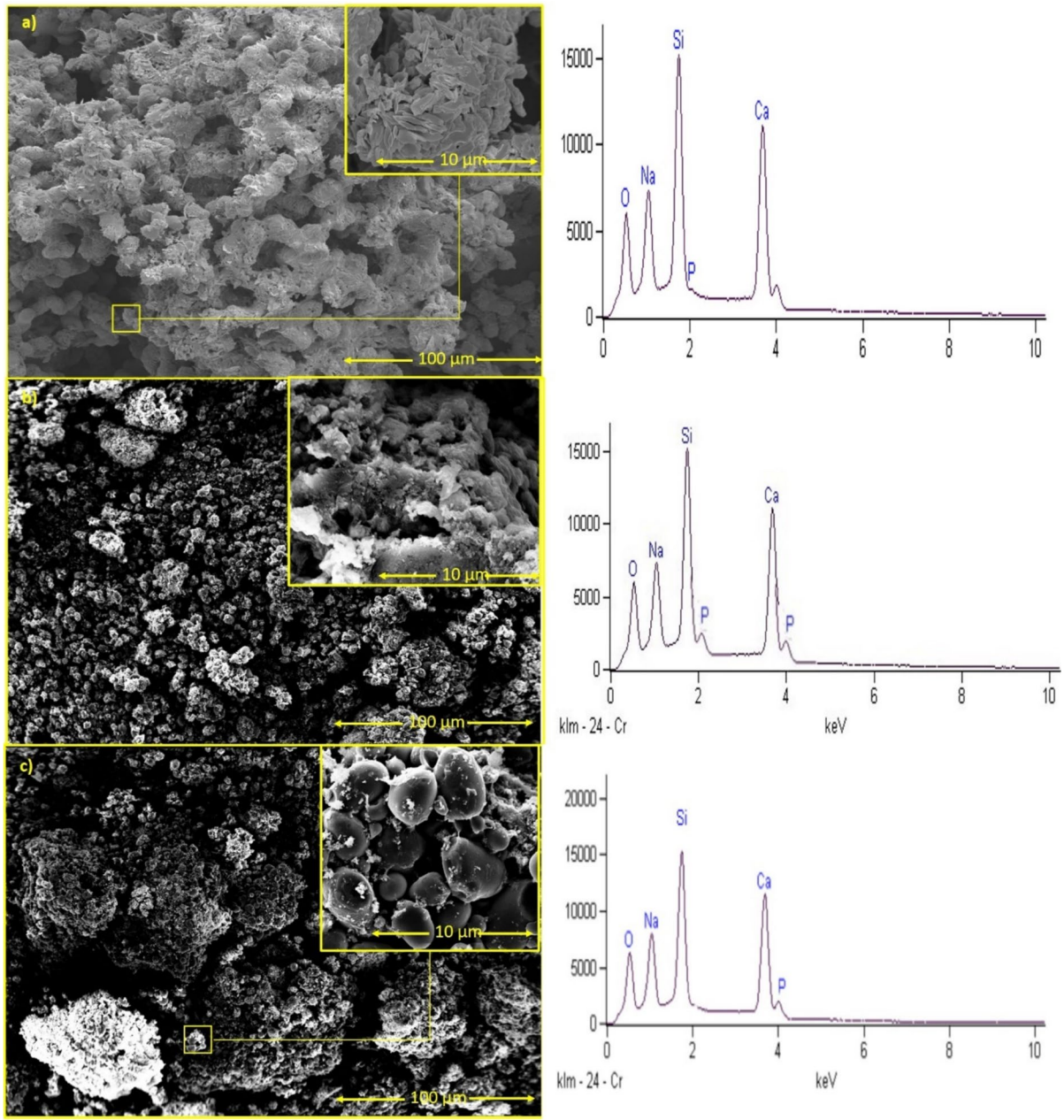

Fig. 3 SEM and EDX of **a** BG **b** CMC5 and **c** CMC10

differences should be interpreted cautiously. The error bars shown in Fig. 4 represent the standard deviation (mean ± s.d.).

This trend may reflect partial particle rearrangement and compaction during the thermal degradation of the CMC template, which facilitates closer packing of the bioglass network. Such behavior suggests that templating with CMC influences scaffold architecture without substantially altering bulk density.

BET analysis (Table 2) revealed that incorporating 5 wt.% CMC into the sol approximately doubled the average pore size while reducing the surface area by ~ 20% compared to 45S5 Bioglass®. The surface areas of BG (5.459 m^2/g) and CMC5

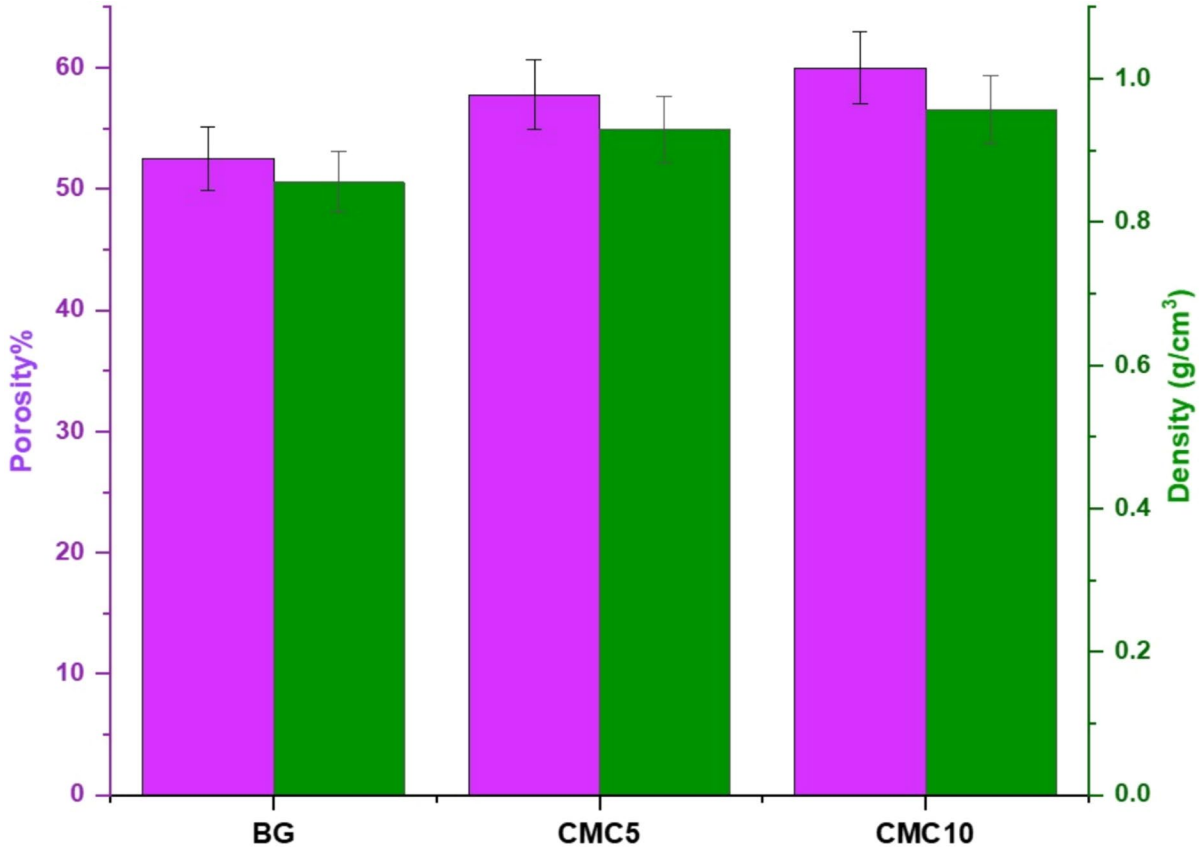

Fig. 4 Porosity and density comparision

Table 2 The results of BET analysis of BG and BG-CMC5 Scaffold

Samples	Surface area (m^2/g)	Total pore volume (cm^3/g)	Pore size (nm)
BG	5.459	0.217	79.50
CMC5	3.836	0.325	169.32

(3.836 m^2/g) remained higher than that of 45S5 Bioglass® (2.7 m^2/g; Jones 2015), indicating that moderate CMC addition enhances pore development without severely compromising surface area. The observed reduction in surface area, despite the increase in pore size, is likely due to partial coalescence or collapse of smaller pores during heat treatment, leading to a more open but less finely structured texture.

According to IUPAC classification, both BG and CMC5 are macroporous structures (Baino et al. 2016). This can be attributed to the sol–gel synthesis route and thermal degradation of the CMC template, which together promote the formation of uniformly sized pores during calcination. Moreover, SEM micrographs (Fig. 3) revealed interconnected macropores (> 100 µm), particularly in CMC5, aligning with the overall porosity range (52–60%) obtained from ethanol displacement. Such macro-architectural features are beneficial for cell infiltration and vascularization, consistent with the structural requirements of cancellous bone scaffolds (Dubey et al. 2021; Szczodra et al. 2023). Click or tap here to enter text. Click or tap here to enter text.

Crystallinity analysis

The XRD patterns of BG, CMC5, and CMC10 scaffolds are presented in Fig. 5a. The diffraction profiles exhibited broad amorphous features together with several low-intensity crystalline reflections, indicating

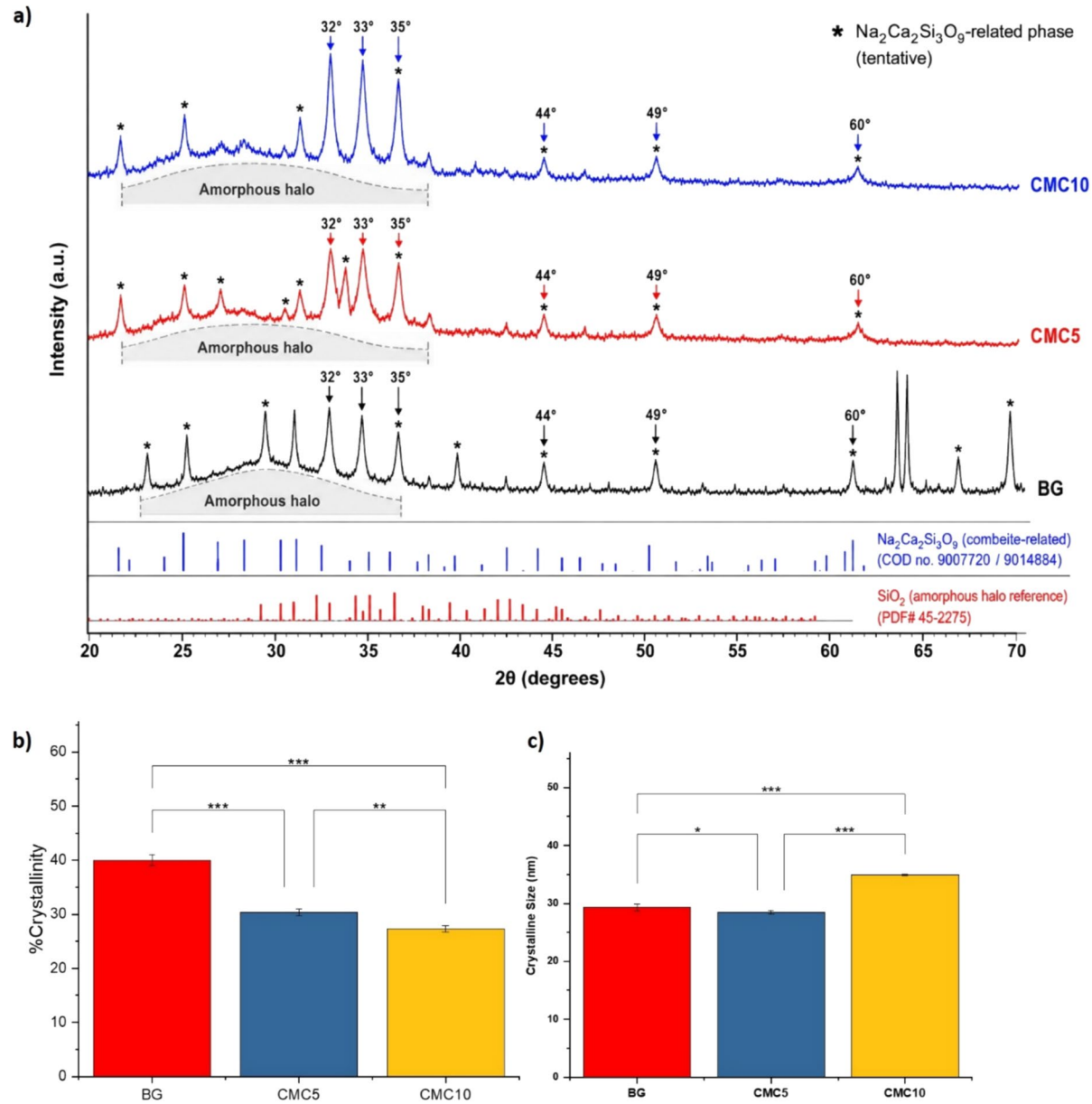

Fig. 5 **a** X-ray diffraction (XRD) patterns of BG, CMC5, and CMC10 scaffolds showing the amorphous halo and crystalline reflections tentatively attributed to $Na_2Ca_2Si_3O_9$-related crystalline domains. The major diffraction features near 32°, 33°, 35°, 44°, 49°, and 60° (2θ) are indicated for clarity. **b** Crystallinity (%). **c** Crystallite size of the fabricated scaffolds. Crystallinity was determined from the ratio of crystalline peak area to the total diffracted area after baseline correction. Statistical analysis was performed using one-way ANOVA with Holm–Bonferroni post-hoc test (n = 3). Data are presented as mean ± standard deviation. $^{*}P \leq 0.05$, $^{**}P \leq 0.01$, and $^{***}P \leq 0.001$

partial crystallization of the bioglass system after heat treatment. A broad diffuse hump was observed between approximately 22° and 37° (2θ), corresponding to the amorphous silica-rich glass network commonly reported for bioactive glass materials (Jones 2015).

Several crystalline reflections were observed near 32–35° (2θ), which are consistent with sodium

Table 3 The crystallinity and crystallite size of BG and BG-CMC samples

Sample name	Crystallinity%	Crystallite size (nm)
BG	40.27 ± 0.15	28.88 ± 2.41
CMC5	30.50 ± 0.57	28.52 ± 0.30
CMC10	27.14 ± 0.35	34.89 ± 0.06

calcium silicate ($Na_2Ca_2Si_3O_9$)-related crystalline domains commonly reported in partially crystallized 45S5-derived bioactive glass systems (Hench and Jones 2015; Sugumaran et al. 2024). However, due to the partially amorphous nature of the samples and the broad diffraction features, the phase assignment was considered tentative. Only the major reproducible peaks were considered for phase interpretation to avoid overestimation of low-intensity statistical noise.

The calculated crystallinity values were approximately 40%, 30%, and 27% for BG, CMC5, and CMC10, respectively (Table 3 and Fig. 5b). The gradual reduction in crystallinity with increasing CMC concentration suggests that the polymeric template inhibited crystal nucleation and growth while promoting retention of the amorphous glassy phase. During thermal decomposition, CMC generates gaseous products and additional porosity within the scaffold structure, thereby increasing structural disorder and limiting long-range atomic rearrangement required for crystal growth. Similar reductions in crystallinity and mixed amorphous/crystalline behavior have also been reported in 45S5 bioactive glass systems prepared under different processing conditions (Sugumaran et al. 2024). Comparable observations were previously reported for porous bioactive glass and glass–ceramic systems containing polymeric pore-forming agents (Wu et al. 2011; Baino et al. 2018).

The crystallite sizes estimated using the Scherrer equation were approximately 29 nm for BG, 28 nm for CMC5, and 35 nm for CMC10 (Table 3 and Fig. 5c). The slightly larger crystallite size observed for CMC10 may be associated with localized crystal coarsening within isolated crystalline regions despite the overall reduction in bulk crystallinity.

Swelling profile

Swelling behavior critically affects scaffold performance by governing fluid transport, nutrient exchange, and degradation kinetics (Aki et al. 2020; Zeitler And Cormack 2006). As shown in

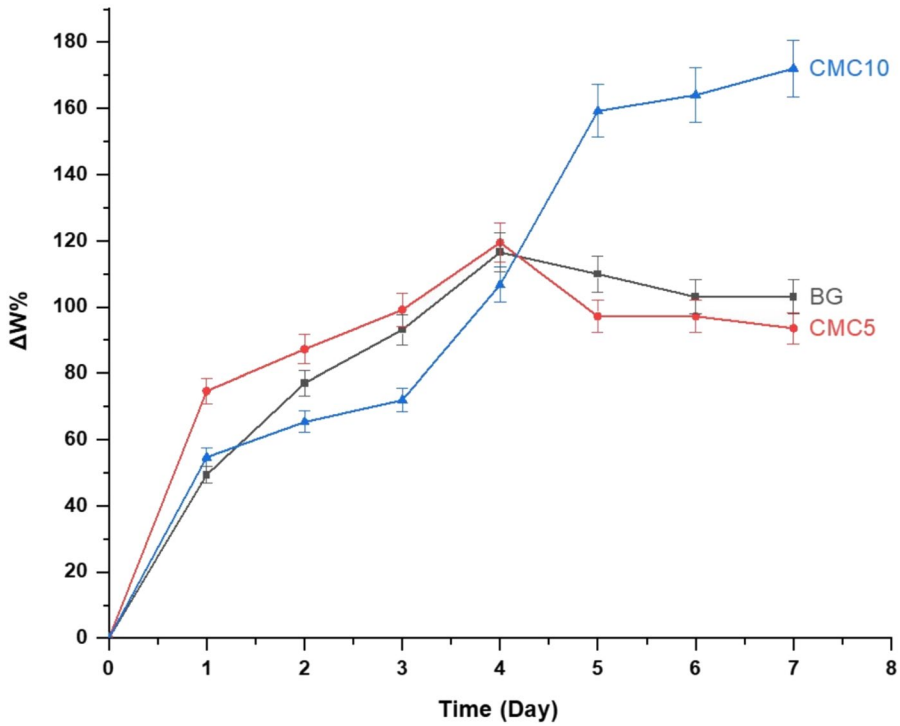

Fig. 6 Swelling profiles of bioglass before and after templating. Statistical tests used were a one-way ANOVA with Holm-Bonferroni post-hoc (n = 3). Values are means ± s.d. for three independent replicates

Fig. 6, BG and CMC5 exhibited the highest water uptake on day 4, with rates of 16.79% and 11.2% per day, respectively, and corresponding discharge rates of 4.5% and 3.6% per day. In contrast, the CMC10 swelled throughout the observation periods at an average rate of 16.67% per day. The markedly higher swelling in CMC10 is attributed to its lower degree of crystallinity and crosslinking, which facilitates greater water penetration into the BG network (Rimpy And Ahuja, 2022). These structural effects enable efficient swelling–deswelling dynamics and enhance fluid convection within the scaffold (Dubey et al. 2021; Szczodra et al. 2023).

Mechanical properties

Mechanical properties are critical for evaluating the regenerative potential of scaffolds, particularly for bone repair. A range of factors including pore size, homogeneity, morphology, and configuration, strongly influence the scaffold's mechanical performance (Dubey et al. 2021). Compressive strength defined as the maximum stress sustained before fracture or a sharp stress drop, is a key indicator of load-bearing capacity (Kane and Roeder 2012). Figure 7a–c presents the stress–strain curves, compressive strength, and Young's modulus for BG, CMC5, and CMC10 scaffolds. The maximum stress values extracted from the curves were 3.07 ± 0.65 MPa (BG), 4.24 ± 0.58 MPa (CMC5), and 8.36 ± 0.72 MPa (CMC10), confirming significant enhancement with CMC addition.

The compressive stress–strain relationship (Fig. 7a) illustrates the elastic behavior of the scaffolds under load, where the samples initially undergo elastic deformation and store energy before fracture. Compressive strength was determined as the maximum stress value before the stress drop on the curve, representing the load-bearing limit of each scaffold. Effective energy dissipation within the interconnected pore structure is essential for maintaining mechanical integrity under compression (Yadav And Maji 2019; Zamani et al. 2019). The maximum compressive strengths recorded from the curves were 3.07 ± 0.65 MPa for BG, 4.24 ± 0.58 MPa for CMC5, and 8.36 ± 0.72 MPa for CMC10, corresponding to strain-to-failure values of approximately 35%, 25%, and 18%, respectively. These results confirm a significant enhancement in mechanical performance with CMC addition, which can be attributed to hydrogen bonding between hydroxyl (–OH) groups of methylcellulose and silanol (Si–OH) groups on the bioglass surface, as well as interchain cross-linking during the sol–gel process (Rimpy and Ahuja, 2022). The compressive strength values of the bioglass scaffold, before and after templating, fall within the compressive strength range of cancellous, trabecular, and tibial bones as shown in Table 4.

SEM analysis (Fig. 3) revealed interconnected macropores (> 100 µm) for both CMC5 and CMC10 scaffolds, consistent with enhanced pore interconnectivity seen in BET results. CMC addition increased the average pore size from 79.5 nm (BG) to 169.3 nm (CMC5), and extrapolated data for CMC10 suggest a further increase to ~ 360 nm, with total pore volume rising to ~ 0.488 cm^3/g and surface area decreasing to ~ 2.69 m^2/g. Such textural evolution improves energy dissipation pathways within the scaffold, thereby sustaining higher compressive stress prior to failure (Eqtesadi et al. 2015).

The elastic modulus is a critical parameter in evaluating the biomechanical performance of a bone implant, as a higher elastic modulus indicates increased resistance to deformation. Matching the scaffold's stiffness with that of the host tissue facilitates stress transfer along the interface zone, leading to stable bonding and osteointegration. The Young's modulus values (Fig. 7c) were 0.21 ± 0.04 MPa (BG), 2.1 ± 0.31 MPa (CMC5), and 5.5 ± 0.45 MPa (CMC10). Generally, the increase in stiffness with higher CMC content is consistent with the observed rise in density and reduced porosity, indicating more compact strut structures and fewer voids for deformation. Matching the scaffold's stiffness with that of cancellous bone facilitates stress transfer and osteointegration (Baino and Fiume 2019; Hu et al. 2017).

In-vitro biomineralization study

Morphology

The bioactivity of bioglass was evaluated using an in-vitro test, where the BG material was immersed in a simulated body fluid (SBF) solution at 37 °C for 28 days. Samplings were collected at specified intervals. The presence of HA was screened by analyzing SEM images of the sample surfaces. Figures 8 and 9 illustrated the formation of the appetite layers

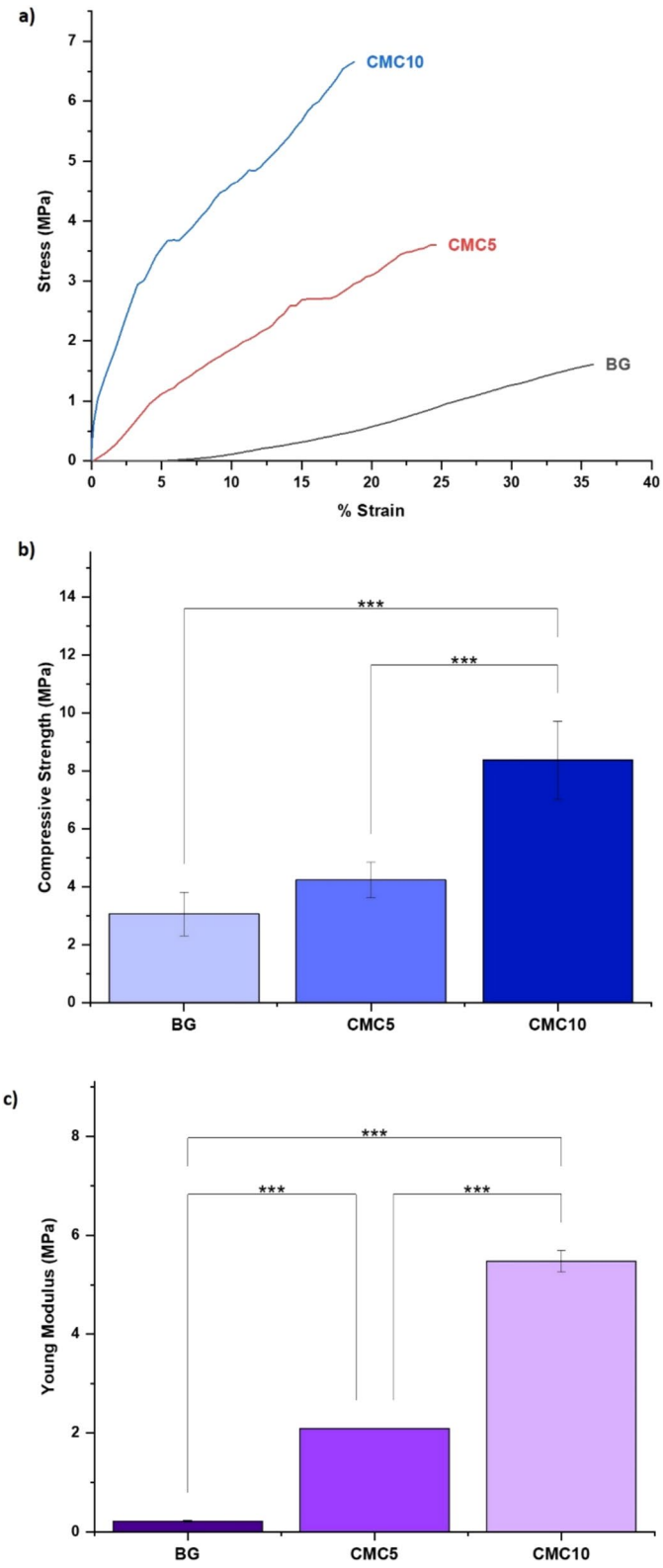

Fig. 7 **a** stress- strain behavior **b** compressive strength and **c** young modulus of the Samples. (n = 5). Statistical tests used were a One-way ANOVA with Holm-Bonferroni post-hoc. Values are means ± s.d. for three independent replicates ***$P \leq 0.001$

Table 4 Compressive strength of BG and BG-CMC scaffolds in comparison with stress ranges of natural bones

Samples	Compressive strength (MPa)	Bone category (stress range, MPa)	References
BG	3.07 ± 0.65	Cancellous bone (1.5–45)	Baino And Fiume 2019; Ramlee et al. 2019; Szczodra et al. 2023
CMC5	4.24 ± 0.58	Cancellous / lower Trabecular bone (2–12)	
CMC10	8.36 ± 0.72	Lower trabecular (2–12)	

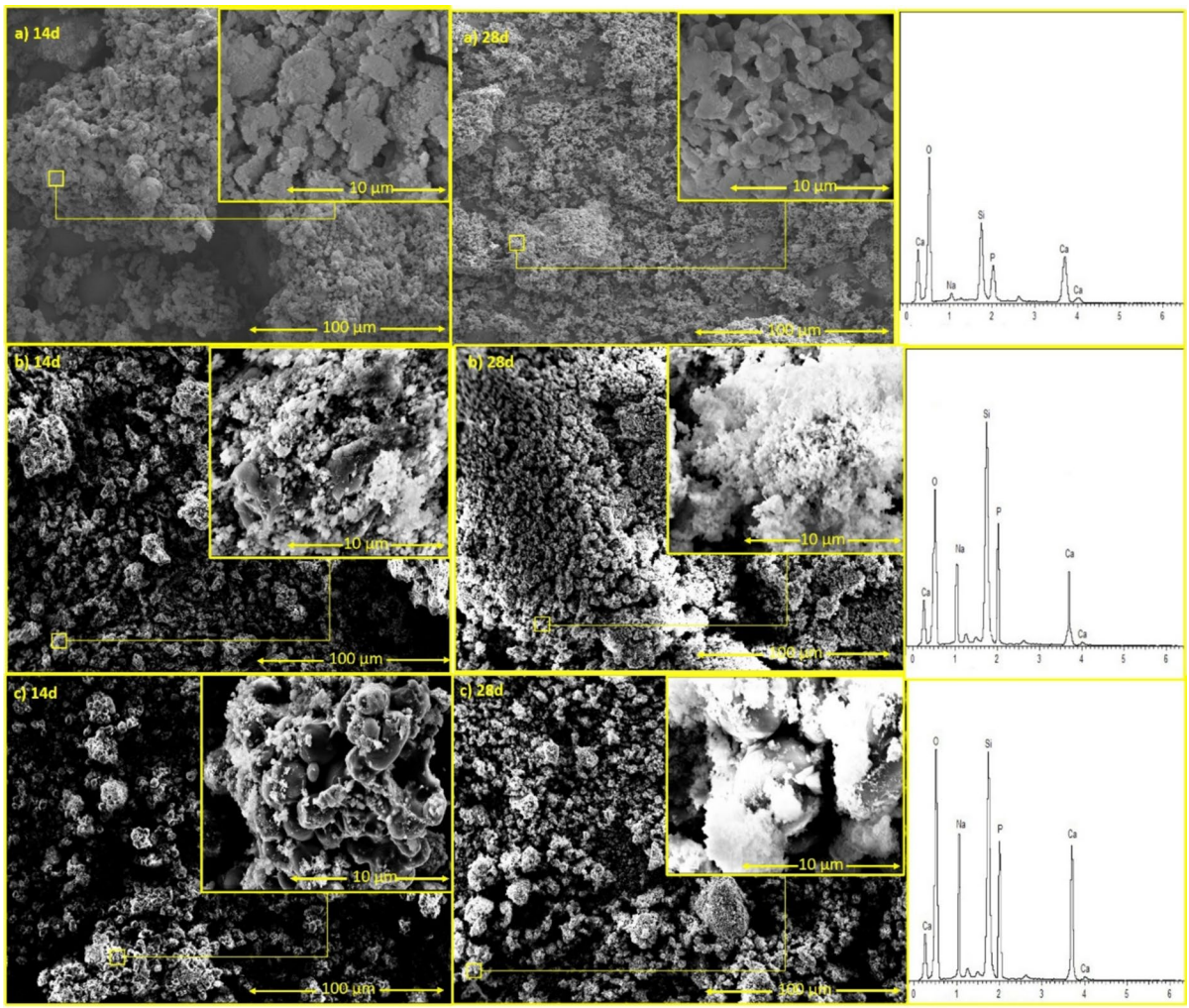

Fig. 8 SEM–EDX images of SBF—non-refreshment (NR-Sample) **a** BG **b** CMC5 **c** CMC10

on the BG and BG-CMC surfaces after immersion in the SBF for 14 days. Both the BG and CMC5 samples exhibited microcracks after 14 days, which were attributed to physical and chemical reactions between the sample surfaces and the SBF solution, primarily driven by water erosion and ion exchange processes (Luo et al. 2016). Additionally, both samples were coated by a non-uniform hydroxyapatite (HA) layer, with the R-sample showing a lower density compared to the NR-sample (Figs. 8a, b and 9a, b). As the mineral layer densified, the HA crystal slowly filled the microcracks. Across all samples, PO_4^{3-} and Ca^{2+} ions

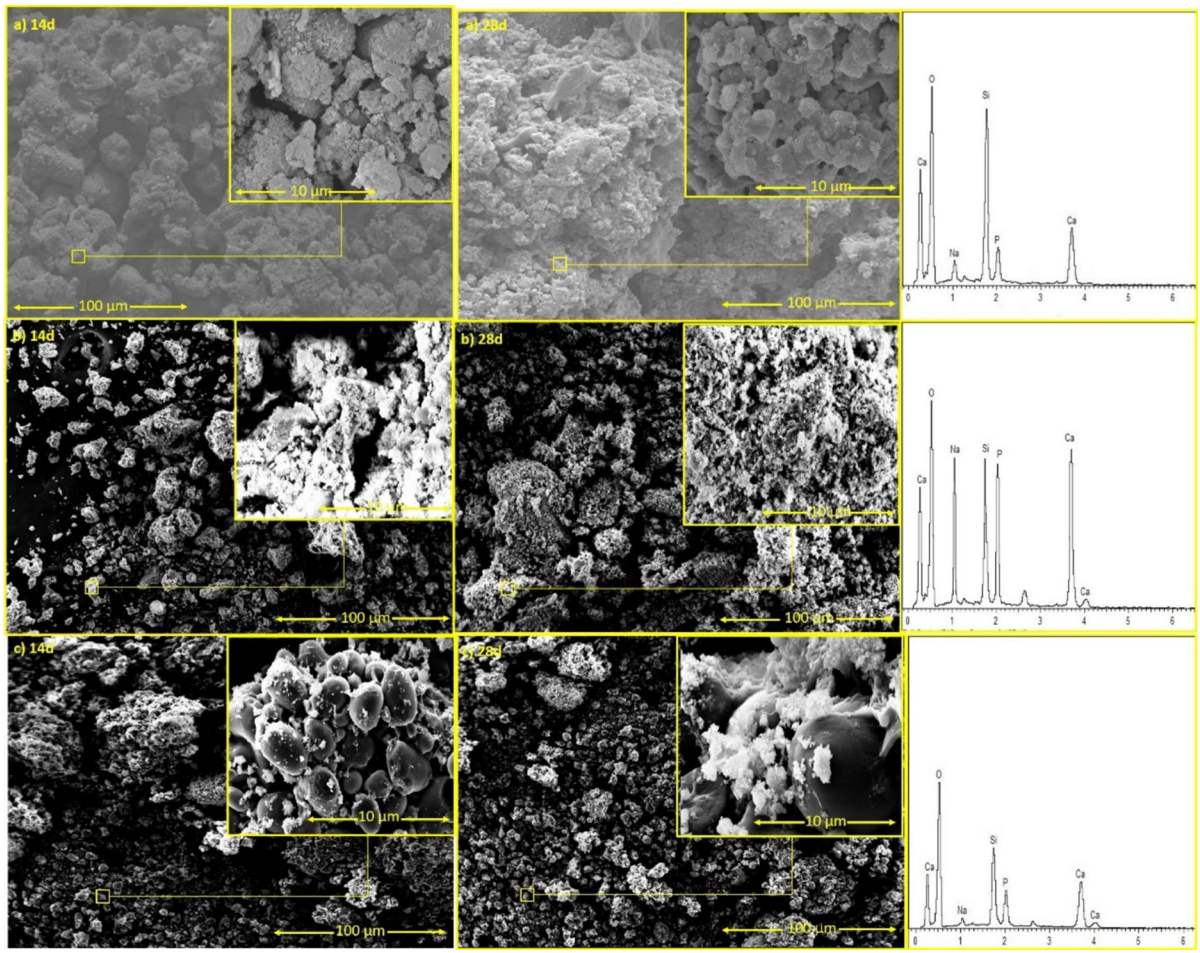

Fig. 9 SEM–EDX images of SBF refreshment (R-Sample) **a** pure BG **b** CMC5 **c** CMC10

diffused through the porous silica gel layer into the simulated body fluid (SBF), leading to ionic supersaturation and the subsequent formation of water-rich $CaO–P_2O_5$ sediments that coated the silica gel layer (Chen et al. 2018). After 28 days of immersion under non-refreshment conditions (NR-Samples), the surfaces of both the BG and CMC5 samples were fully covered with HA crystals (Fig. 8a), with CMC5 sample exhibited a denser and more uniform HA layer compared to BG and CMC10 (Fig. 8b).

In contrast, under constant pH conditions (R-samples), none of the samples developed a fully dense HA coating (Fig. 9). This suggests that while pH stabilization may promote HA formation, the development of a continuous and stable layer likely requires a longer immersion period (López-Ortiz et al. 2020; Sarmast Sh et al. 2023). Furthermore, CMC10 exhibited minimal HA deposition under both NR and R conditions, indicating that the surface characteristics of CMC10 samples which are bulky and dense inhibited the nucleation and growth of HA crystals (Eqtesadi et al. 2015). Since the rate of mineral deposition is closely associated with the material's bioactivity, the reduced HA formation on CMC10 reflects its lower bioactivity (Gupta and Santhiya 2017; Moghanian et al. 2021).

Energy-dispersive X-ray (EDX) analysis after 28 days in SBF (Figs. 8 and 9) confirmed the formation of bone-like apatite, as evidenced by the presence of Si, P, Ca, and O peaks. The stoichiometric Ca/P ratio of natural HA ($Ca_5(PO_4)_3(OH)$) is 1.67 (Hu et al. 2022). Over time, the accumulation of Ca and P ions on the glass surface supports the formation of bioactive mineral phases conducive to bone

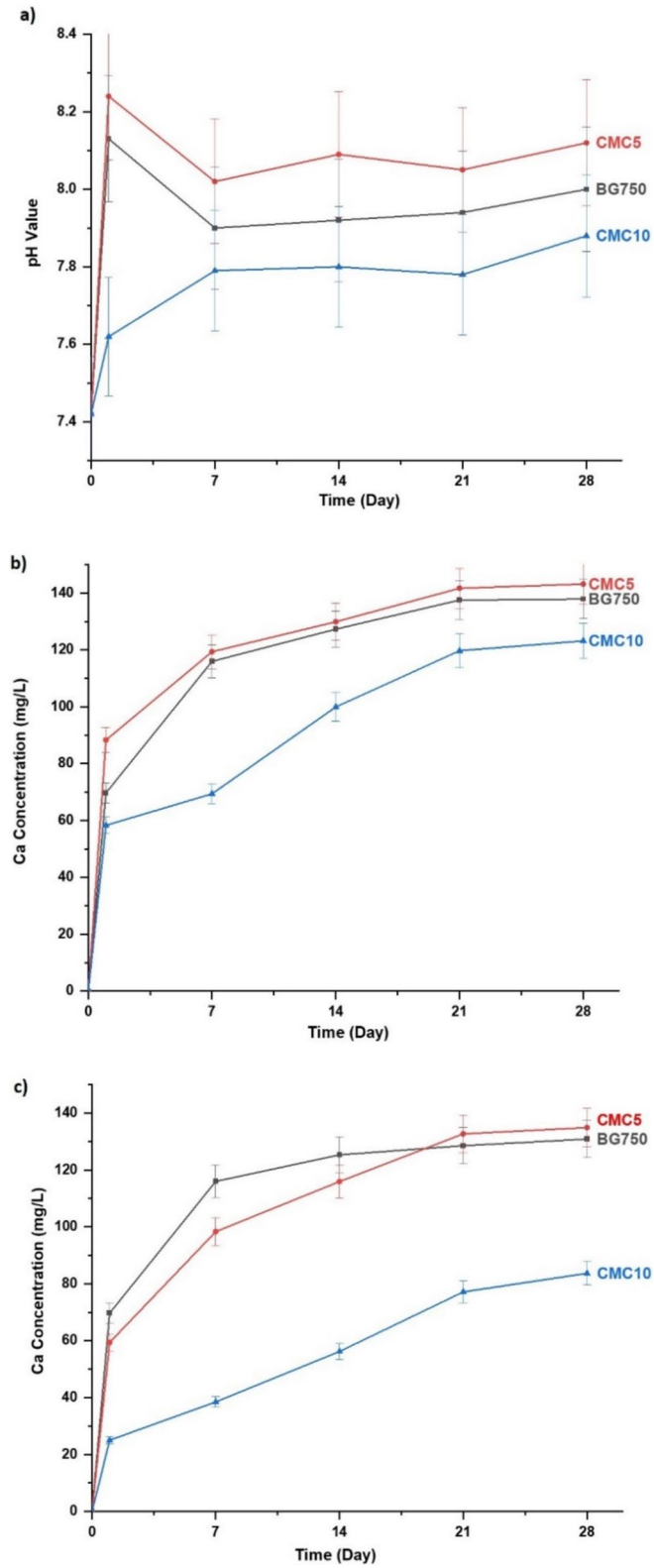

Fig. 10 **a** pH evaluations profile **b** Ca concentration of NR- sample **c** Ca concentration of R-sample after immersion in SBF for 28 days

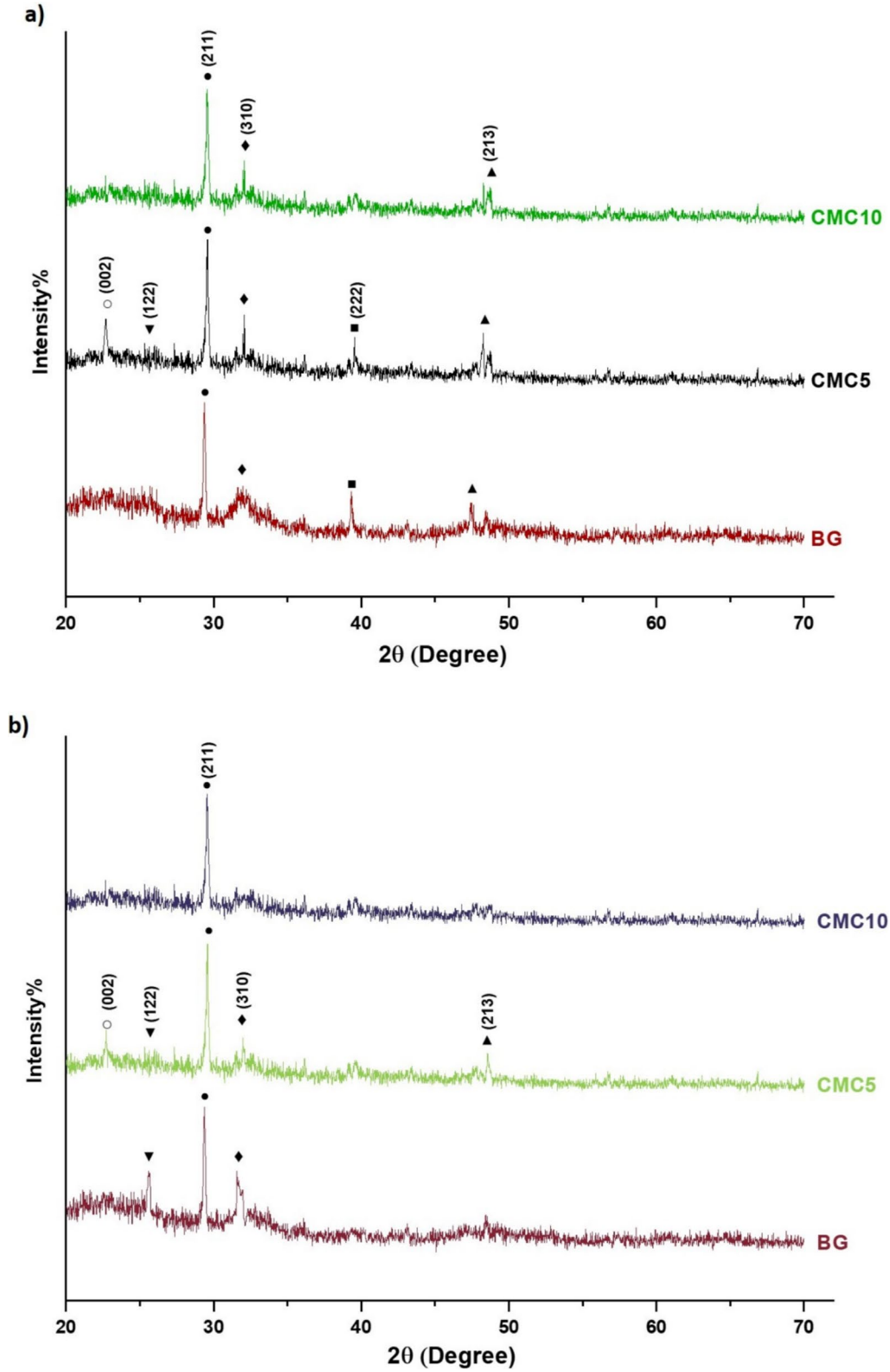

Fig. 11 XRD of **a** NR-samples **b** R-samples incubated in simulated body fluid for 28 days

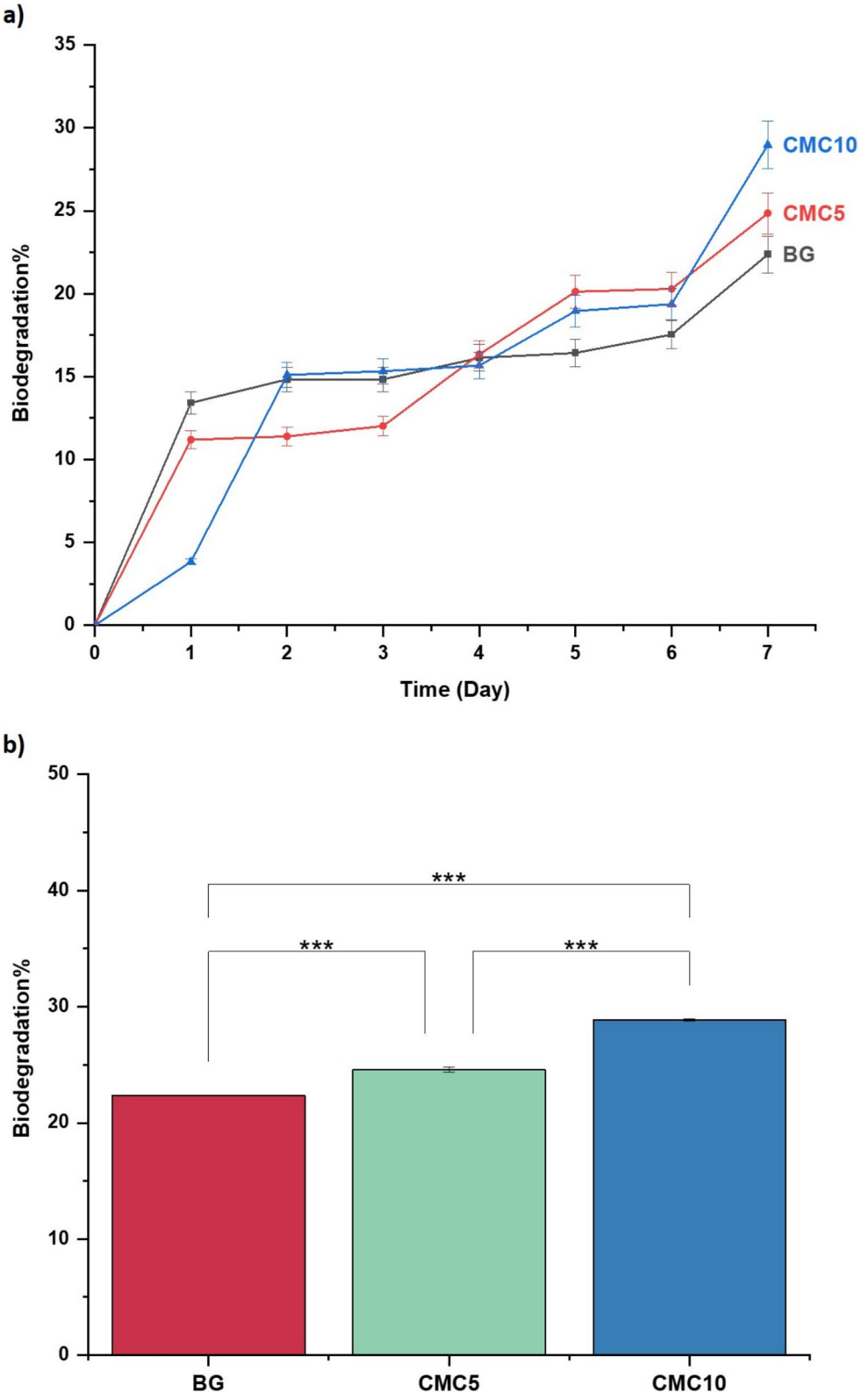
a)
Biodegradation%
Time (Day)
CMC10
CMC5
BG
b)
Biodegradation%
***
***
***
BG
CMC5
CMC10

◂**Fig. 12** **a** The biodegradation rate of BG and BG-templated samples within 7 days. **b** The average of weight loss after 7 days. Statistical tests used were a One-way ANOVA with Holm-Bonferroni post-hoc (n = 3). Values are means ± s.d. for three independent replicates. ***$P \leq 0.001$

Table 5 Ca/P ratio of HA layer formation after 28 days immerssion in SBF solution

Ca/P Ratio		
Sample name	NR- samples	R- samples
BG	1.65	1.62
CMC5	1.68	1.64
CMC10	1.37	1.25

regeneration. The Ca/P ratios for the samples, presented in Table 4, highlight the significant influence of CMC templating on calcium-phosphate deposition. Notably, the CMC5 sample exhibited a higher Ca/P ratio, indicating enhanced uptake of calcium and phosphate ions from the SBF and promoting more robust HA formation compared to other samples. Overall, NR samples demonstrated higher Ca/P ratios than their R counterparts, which can be attributed to the absence of SBF refreshment and the resulting gradual pH increase. This condition likely facilitated prolonged ion exchange and allowed sufficient time for the transformation of newly deposited mineral phases into a denser, more stable HA layer (López-Ortiz et al. 2020; Sarmast Sh et al. 2023).

Evaluation of pH values and ion concentration

Figure 10a illustrates the pH variation of NR-Samples during the immersion time. The NR samples exhibited pH variation (ΔpH) ranging from 0.46 to 0.82. BG and CMC5 samples showed a sharp pH increase within the first seven days, followed by a transient drop on day 7 and a gradual rise over the subsequent three weeks. In contrast, CMC10 displayed an initial increase, fluctuating between days 7 and 21, before reaching its peak in the final week. These fluctuations are attributed to differences in the Ca^{2+} ions release among the samples (Anand et al. 2022; Luo et al. 2022).

Figure 10b shows that the calcium ion release profiles of BG and CMC5 under non-refreshment (NR) conditions closely resemble those of 45S5 Bioglass®, supporting its use as a reference material (Wajda And Sitarz 2018). The alignment between calcium ion concentration and pH trends suggests a strong correlation, likely due to the disordered atomic structure of sol–gel-derived bioglass, which facilitates ion release compared to crystalline materials (Li et al. 2019). Among the NR samples, CMC5 exhibited the highest Ca^{2+} release, attributed to its enhanced porosity and surface area resulting from templating process (Ramlee et al. 2019).

In contrast, R-samples showed lower initial Ca^{2+} concentrations (Fig. 10c), with a gradual increase over time. While BG maintained a similar trend to its NR counterpart, CMC5 and CMC10 displayed a steady rise in ion release throughout the 28 day period. All samples reached a near-constant Ca^{2+} release rate during the final week. These findings indicate that constant pH conditions promote sustained ion diffusion but may delay the formation of a dense HA layer. XRD analysis supports this, showing that while constant pH facilitates $CaO–P_2O_5$ layer formation, it may inhibit complete HA crystallization within 28 days. This suggests that the initial stages of the bone-bonding process occur within this timeframe for BG and CMC5 under NR conditions (Luo et al. 2022). CMC10 exhibited distinct behavior compared to other samples, showing the lowest pH and calcium ion variation in both NR and R groups. Unlike BG and CMC5, CMC10 did not follow the expected progression of the initial four stages of the bone-bonding process within the 28 day period. This deviation is likely due to its lower porosity and smoother surface, which limit ion exchange and hinder HA formation. Additionally, reduced calcium availability from the bulk material may further restrict HA layer development, resulting in higher residual calcium ion concentrations in the surrounding medium (Hu et al. 2022; Luo et al. 2022).

Crystallinity analysis

Figure 11 presents the XRD patterns of NR and R samples. Comparison with the Joint Committee on Powder Diffraction Standards (JCPDS #09–0432) confirms the presence of hydroxyapatite (HA) phases, with diffraction peaks observed between $2\theta = 20°$ and 70°. Characteristic reflections at $2\theta = 24°$, 26°, 29°, and 32° correspond to the (002), (122), (211), and (310) planes of HA, while additional peaks at $2\theta = 39°$ and 49° represent the (222) and (213) planes,

indicating the formation of stable HA crystals (Hu et al. 2022; Sarmast Sh et al. 2023).

Both NR and R groups exhibited (211) and (310) peaks across all samples. However, the (002) and (122) peaks were exclusive to CMC5 in both groups, while the (222) peak appeared only in BG and CMC5 under NR conditions. Notably, the (213) peak was present in all NR samples but was detected only in CMC5 among the R samples. These findings suggest that HA formation did not strictly follow ideal stoichiometric conditions. Nevertheless, the presence of additional HA reflections in CMC5 indicates that templating with 5% CMC enhances bioactivity and promotes the development of a more robust and stable HA layer under both static and pH-controlled conditions. Conversely, maintaining a constant pH of 7.42 introduced a more complex environment for BG samples, potentially due to the presence of additional ions or molecules within the crystalline lattice or on the surface. Under these conditions, the reaction favored acidic environments, promoting the stoichiometric formation of the monoclinic phase, which contributes to the stabilization of HA structures commonly found in bone tissue (López-Ortiz et al. 2020; Sarmast Sh et al. 2023). SEM and EDX analyses confirmed the development of an HA layer in these samples. However, the robust HA layer observed on BG and CMC10 under constant pH conditions (R-samples) was not consistently reproduced. This suggests that SBF rehydration and pH stabilization may extend the time required for the transformation of initial mineral deposits into a dense and stable HA layer (López-Ortiz et al. 2020; Sarmast Sh et al. 2023; Xiao et al. 2022).

In-vitro degradation study

Figure 12a shows the degradation profiles of BG and CMC samples after one week of immersion in PBS at pH 7.4. CMC5 and CMC10 exhibited more weight loss than BG, indicating higher degradation rates. BG showed the highest degradation on day 1, remained stable through day 6, and increased again on day 7. CMC5 displayed fluctuating degradation, with significant mass loss on days 4 and 5. CMC10 showed the most rapid degradation within the first two days, followed by fluctuations and a final increase on day 7. After one-week, cumulative weight loss was approximately 22% for BG, 25% for CMC5, and 29% for CMC10.

These results highlight the influence of porosity and surface morphology on degradation behavior. The higher degradation in templated samples is attributed to increased porosity and surface area, which enhance fluid penetration and ion exchange. Controlling the degradation rate is critical for maintaining scaffold stability and aligning degradation with new bone formation (Dubey et al. 2021). Tailoring scaffold properties can help balance degradation and swelling behavior to optimize performance in bone tissue engineering applications (Rimpy And Ahuja 2022).

In-vitro antibacterial evaluation

The antibacterial activity of BG, CMC5 and CMC10 was evaluated against *Staphylococcus aureus* and *Escherichia coli* (Hu et al. 2022). The silicate-based bioglasses, such as 45S5 Bioglass®, exhibit antibacterial properties through mechanisms such as pH elevation, increased osmotic pressure, and physical disruption of bacterial membranes by sharp particles. The release of Si, Ca, PO_4^{3-}, and Na^+ ions into the surrounding medium raises pH and osmotic pressure, while calcium and alkali ions disrupt bacterial membrane potential, collectively inhibiting bacterial growth (Anand et al. 2022; Moghanian et al. 2021).

As shown in Table 6 and Fig. 13, all samples demonstrated excellent antibacterial efficacy against *E. coli* than *S. aureus*, likely due to differences in cell wall structure between Gram-negative and Gram-positive bacteria (Ciołek et al. 2019; Zamani et al. 2019). Among the samples, CMC10 exhibited the lowest antibacterial activity. While BG and CMC5 showed similar inhibition against E. *coli*, CMC5 achieved approximately 10% higher inhibition against *S. aureus* compared to BG. This enhanced performance is attributed to the increased release of Ca^{2+} ions from the CMC5 scaffold, which contributed to its superior antibacterial efficacy (Table 5).

In-vitro biological evaluation

Figure 14 shows the quantitative MTT results. A significant increase in viability ($P < 0.001$) was observed for the 25% extracts of BG and CMC5, with cell viability > 90%, while CMC10 showed lower values. All samples exceeded 70% viability at this dilution, confirming their "nontoxic" classification. Although CMC10 possesses high overall porosity and interconnectivity, its larger crystallite size and reduced

surface area (as indicated by BET analysis) can limit initial cell adhesion, leading to slightly reduced viability (Szczodra et al. 2023). In contrast, the moderate pore size and higher surface area of BG and CMC5 provided a more favorable substrate for cell attachment and proliferation. The reduced viability observed in the 100% extract is attributed to rapid alkali ion release and transient pH increases in vitro (Rezaeipour et al. 2023). However, under physiological conditions, buffering by body fluids mitigates these effects. Thus, the high cell viability observed at 25 and 50% extract concentrations confirms the intrinsic biocompatibility of BG and CMC5 scaffolds and supports their potential for safe implantation.

Conclusion

This study presents an alternative templating approach using sodium methylcellulose (CMC) with varying weight per volume percentages (5 and 10) to create a porous SiO_2–CaO–P_2O_5–Na_2O bioglass via the sol–gel method. The addition of CMC significantly influenced the morphology and porosity of the bioglass samples. The CMC5 sample exhibited high porosity (56%), larger pore size (169 nm), and increased total pore volume (0.325 cm^3/g) compared to the BG sample. This can be attributed to the influence of CMC on the sol–gel process and gelation of the bioglass matrix. Additionally, the

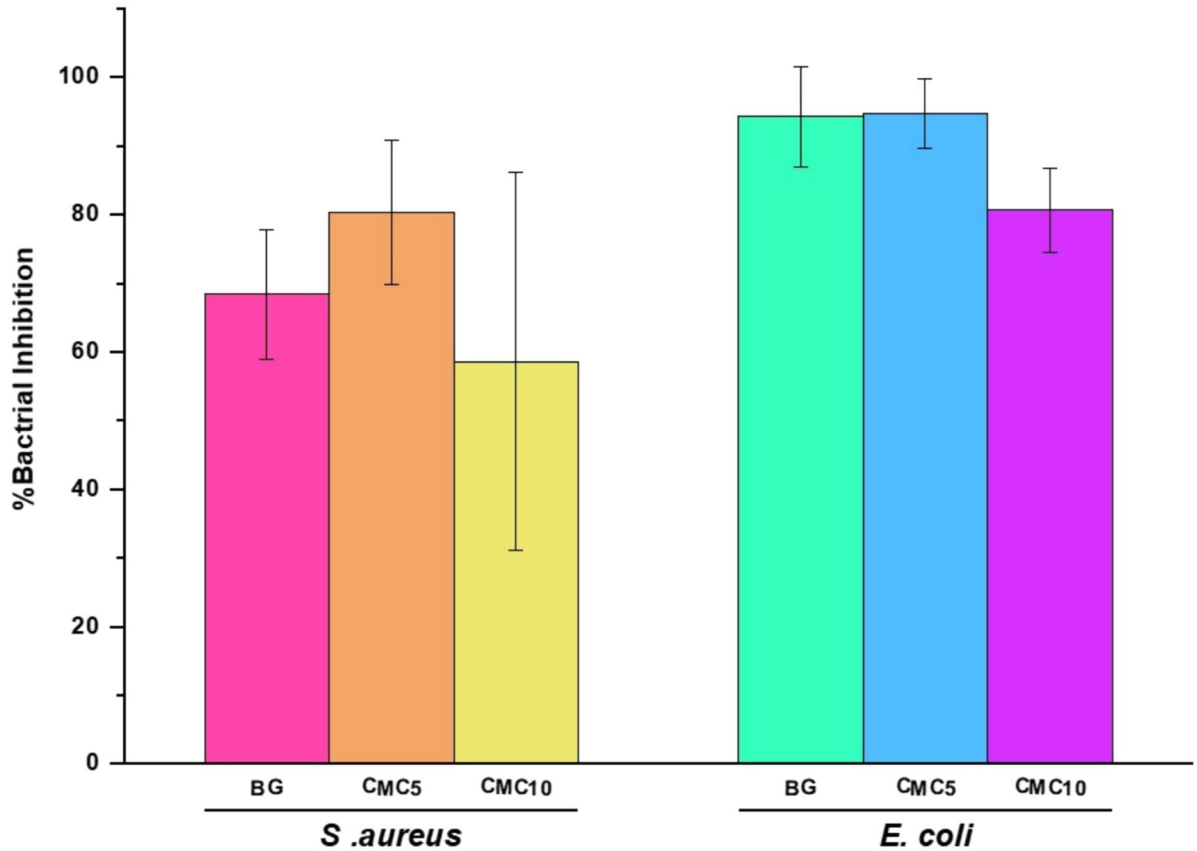

Fig. 13 Bacterial inhibition of *E. coli* and *S. aureus* (n = 3). Statistical tests used were a one-way ANOVA with Holm-Bonferroni post-hoc. $P < 0.05$

Table 6 pH changes during bacteria inhibition

	S. aureus		*E. coli*	
Sample name	Initial pH	Final pH	Initial pH	Final pH
BG	6.71 ± 0.22	9.76 ± 0.18	6.75 ± 0.10	9.76 ± 0.14
CMC5	6.71 ± 0.22	9.92 ± 0.42	6.75 ± 0.10	9.80 ± 0.51
CMC10	6.71 ± 0.22	9.35 ± 0.20	6.75 ± 0.10	9.68 ± 0.17

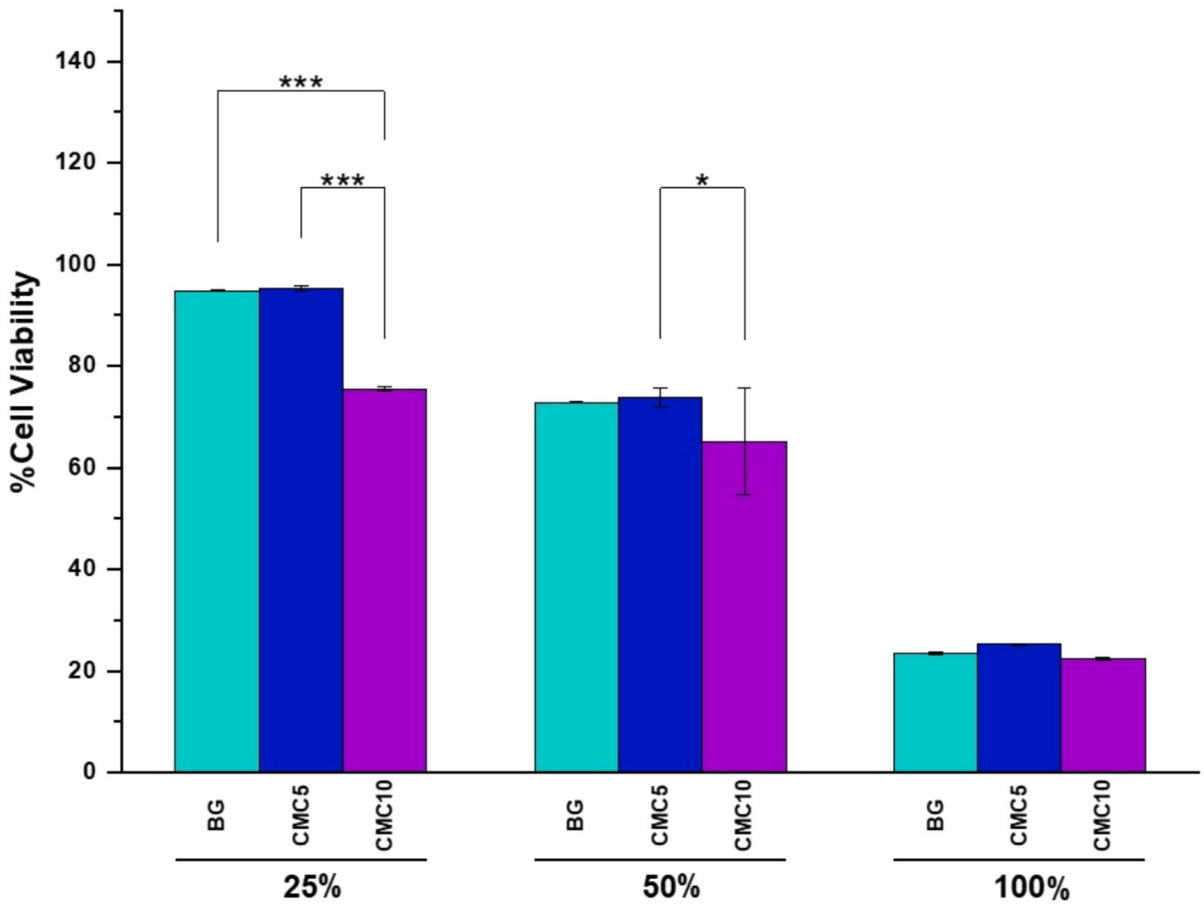

Fig. 14 Percentage viability of 3T3 cultured with 25%, 50% and 100% extraction of bioglass samples in 18 h. Statistical tests used were a One-way ANOVA with Holm-Bonferroni post-hoc. ***$P < 0.001$ and *$P < 0.05$

CMC5 sample demonstrated excellent in-vitro bioactivity by forming a more stable HA layer when immersed in SBF and exhibiting the highest antibacterial efficiency. Furthermore, the templating process led to remarkable enhancements in the compressive strength and elastic modulus values of the produced bioglass, rendering it suitable for cancellous bone applications. The biocompatibility of all samples was confirmed through MTT assay assessment, indicating high cell viability and proliferation for BG and CMC5. Consequently, these findings contribute to the utilization of the templating approach with a 5 wt.% CMC template, presenting a promising method for synthesizing porous

bioactive glass materials. This development holds potential for bone tissue engineering applications.

Acknowledgments The work was funded by Universiti Putra Malaysia under Geran Putra Inisiatif Siswazah (9669500). All chemical analyses were conducted at the Material Characterization Laboratory, Faculty of Engineering, Universiti Putra Malaysia. The sintering processes and microscopic analyses were performed at the Institute of Nanomaterial and Nanotechnology, Universiti Putra Malaysia. The biological analysis was conducted at the Cancer Research Laboratory, Institute of Bioscience, Universiti Putra Malaysia.

Author contribution Maryam Sarmast Shoushtari: Writing—original draft, Software, Project administration, Methodology, Investigation, Formal analysis, Data curation. A.B. Dayang Radiah: Writing—review & editing, Supervision, Funding acquisition. David. Hoey: Writing—review & editing, Validation, Formal analysis. Norhafizah. Abdullah:Investigation. Halimatun.S. Zainuddin: Methodology. Suryani. Kamarudin: Validation.

Funding Open access funding provided by The Ministry of Higher Education Malaysia and Universiti Putra Malaysia. The project was also partially funded by Universiti Putra Malaysia under the Geran Putra Inisiatif (9756200).

Data availability No datasets were generated or analysed during the current study.

Declarations

Conflict of interest The authors declare that there is no conflict of interest regarding the publication of this paper.

References

Ajiz HA, Santoso K, Purnama JA, Widiyastuti W, Nurtono T, Setyawan H (2023) Preparation of monodisperse ZnO/SiO2 composite particles using spray drying with an anionic surfactant template and their photoluminescence characteristics. Adv Powder Technol 34(10):104181. https://doi.org/10.1016/J.APT.2023.104181

Aki D, Ulag S, Unal S, Sengor M, Ekren N, Lin CC, Yılmazer H, Ustundag CB, Kalaskar DM, Gunduz O (2020) 3D printing of PVA/hexagonal boron nitride/bacterial cellulose composite scaffolds for bone tissue engineering. Mater des 196:109094. https://doi.org/10.1016/j.matdes.2020.109094

Albar AA, Ajiz HA, Widiyastuti W, Setyawan H, Nurtono T, Joni IM (2023) The study of silica morphologies generated in spray dried systems. AIP Conf Proc 2623(1):020010. https://doi.org/10.1063/5.0129809

Anand A, Sengupta S, Kaňková H, Švančárková A, Beltrán AM, Galusek D, Boccaccini AR, Galusková D (2022) Influence of copper-strontium co-doping on bioactivity, cytotoxicity and antibacterial activity of mesoporous bioactive glass. Gels 8(11):743. https://doi.org/10.3390/gels8110743

Babaluei M, Mottaghitalab F, Seifalian A, Farokhi M (2023) Injectable multifunctional hydrogel based on carboxymethylcellulose/polyacrylamide/polydopamine containing vitamin C and curcumin promoted full-thickness burn regeneration. Int J Biol Macromol 236:124005. https://doi.org/10.1016/J.IJBIOMAC.2023.124005

Baino F, Fiume E (2019) Elastic mechanical properties of 45S5-based bioactive glass-ceramic scaffolds. Materials. https://doi.org/10.3390/ma12193244

Baino F, Fiorilli S, Vitale-Brovarone C (2016) Bioactive glass-based materials with hierarchical porosity for medical applications: review of recent advances. Acta Biomater 42:18–32. https://doi.org/10.1016/j.actbio.2016.06.033

Baino F, Hamzehlou S, Kargozar S (2018) Bioactive Glasses: Where Are We and Where Are We Going. J Funct Biomat 9(1):25. https://doi.org/10.3390/jfb9010025

Bi D, Chen G, Cheng J, Wen J, Pei N, Zeng H, Li Y (2020) Boswellic acid captivated hydroxyapatite carboxymethyl cellulose composites for the enhancement of chondrocytes in cartilage repair. Arab J Chem 13(6):5605–5613. https://doi.org/10.1016/j.arabjc.2020.03.030

Chen J, Zeng L, Chen X, Liao T, Zheng J (2018) Preparation and characterization of bioactive glass tablets and evaluation of bioactivity and cytotoxicity in vitro. Bioact Mater 3(3):315–321. https://doi.org/10.1016/j.bioactmat.2017.11.004

Ciołek L, Biernat M, Jaegermann Z, Zaczyńska E, Czarny A, Jastrzębska A, Olszyna A (2019) The studies of cytotoxicity and antibacterial activity of composites with ZnO-doped bioglass. Int J Appl Ceram Technol 16(2):541–551. https://doi.org/10.1111/ijac.13144

Ciapetti G, Cenni E, Pratelli L, Pizzoferrato A (1993) In vitro evaluation of cell/biomaterial interaction by MTT assay. Biomaterials 14(5):359–364

Dubey S, Mishra R, Roy P, Singh RP (2021) 3-D macro/microporous-nanofibrous bacterial cellulose scaffolds seeded with BMP-2 preconditioned mesenchymal stem cells exhibit remarkable potential for bone tissue engineering. Int J Biol Macromol 167:934–946. https://doi.org/10.1016/j.ijbiomac.2020.11.049

Dutta RC, Dey M, Dutta AK, Basu B (2017) Competent processing techniques for scaffolds in tissue engineering.

Biotechnol Adv 35(2):240–250. https://doi.org/10.1016/j.biotechadv.2017.01.001. (**Elsevier Inc.**)

Eqtesadi S, Motealleh A, Pajares A, Miranda P (2015) Effect of milling media on processing and performance of 13–93 bioactive glass scaffolds fabricated by robocasting. Ceram Int 41(1):1379–1389. https://doi.org/10.1016/j.ceramint.2014.09.071

Guan J, Fujimoto KL, Sacks MS, Wagner WR (2005) Preparation and characterization of highly porous, biodegradable polyurethane scaffolds for soft tissue applications. Biomaterials 26(18):3961–3971. https://doi.org/10.1016/j.biomaterials.2004.10.022

Gupta N, Santhiya D (2017) Role of cellulose functionality in bio-inspired synthesis of nano bioactive glass. Mater Sci Eng C Mater Biol Appl 75:1206–1213. https://doi.org/10.1016/j.msec.2017.03.026

Gupta N, Santhiya D, Aditya A, Badra K (2015) Dendrimer templated bioactive glass-ceramic nanovehicle for gene delivery applications. RSC Adv 5(70):56794–56807. https://doi.org/10.1039/C5RA04441C

Haghighi FD, Beidokhti SM, Najaran ZT, Sahebian Saghi S (2021) Highly improved biological and mechanical features of bioglass-ceramic/ gelatin composite scaffolds using a novel silica coverage. Ceram Int. https://doi.org/10.1016/j.ceramint.2021.01.274

Hu D, Qiang T, Wang L (2017) Quaternized chitosan/polyvinyl alcohol/sodium carboxymethylcellulose blend film for potential wound dressing application. Wound Mede 16:15–21. https://doi.org/10.1016/J.WNDM.2016.12.003

Hu Y, Thalangamaarachchige VD, Acharya S, Abidi N (2018) Role of low-concentration acetic acid in promoting cellulose dissolution. Cellulose 25(8):4389–4405. https://doi.org/10.1007/s10570-018-1863-7

Hu S, Yang X, Wu H, He D, Zhu Z, Ke G, Zhu J, Cheng X, Wang X (2022) Lotus sprout-templated porous cobalt-doped borate bioglass with antibacterial properties and multiple-layered osteogenic promotion. Appl Mater Today 29:101678. https://doi.org/10.1016/J.APMT.2022.101678

Huang J, Wu D, Liu W, Sun J, Zhao X, Zhang Y, Feng Y (2024) Polyelectrolyte complex gels used for CO absorption. J Polym Sci 62(14):3275–3286. https://doi.org/10.1002/pol.20230555

Jones JR (2015) Review of bioactive glass: from Hench to hybrids. Acta Biomater 23(S):S53–S82. https://doi.org/10.1016/j.actbio.2015.07.019

Kane RJ, Roeder RK (2012) Effects of hydroxyapatite reinforcement on the architecture and mechanical properties of freeze-dried collagen scaffolds. J Mech Behav Biomed Mater 7:41–49. https://doi.org/10.1016/j.jmbbm.2011.09.010

Kokubo T, Takadama H (2006) How useful is SBF in predicting in vivo bone bioactivity? Biomaterials 27(15):2907–2915. https://doi.org/10.1016/j.biomaterials.2006.01.017

Lei B, Chen X, Han X, Zhou J (2012) Versatile fabrication of nanoscale sol-gel bioactive glass particles for efficient bone tissue regeneration. J Mater Chem 22(33):16906–16913. https://doi.org/10.1039/c2jm31384g

Li L, Hu H, Zhu Y, Zhu M, Liu Z (2019) 3D-printed ternary SiO_2 [sbnd]CaO[sbnd]P_2O_5 bioglass-ceramic scaffolds with tunable compositions and properties for bone regeneration. Ceram Int 45(8):10997–11005. https://doi.org/10.1016/j.ceramint.2019.02.183

López-Ortiz S, Mendoza-Anaya D, Sánchez-Campos D, Fernandez-García ME, Salinas-Rodríguez E, Reyes-Valderrama MI, Rodríguez-Lugo V (2020) The pH effect on the growth of hexagonal and monoclinic hydroxyapatite synthesized by the hydrothermal method. J Nanomater 2020:5912592. https://doi.org/10.1155/2020/5912592

Luo H, Ji D, Li W, Xiao J, Li C, Xiong G, Zhu Y, Wan Y (2016) Constructing a highly bioactive 3D nanofibrous bioglass scaffold via bacterial cellulose-templated sol-gel approach. Mater Chem Phys 176:1–5. https://doi.org/10.1016/j.matchemphys.2016.03.029

Luo L, Gong W, Yang X, Qin X, Liu W, Liu L, Ji L (2022) Preparation of super-long aligned mesoporous bioactive glass tubes by an aligned porous polystyrene template. Mater Today Commun. https://doi.org/10.1016/j.mtcomm.2022.103309

Moghanian A, Nasiripour S, Hosseini SM, Hosseini SH, Rashvand A, Ghorbanoghli A, Pazhouheshgar A, Sharifian Jazi F (2021) The effect of Ag substitution on physico-chemical and biological properties of sol-gel derived 60%SiO_2–31%CaO–4%P_2O_5–5%TiO_2 (mol%) quaternary bioactive glass. J Non-Cryst Solids 560:120732. https://doi.org/10.1016/j.jnoncrysol.2021.120732

Mukundan LM, Nirmal R, Vaikkath D, Nair PD (2013) A new synthesis route to high surface area sol gel bioactive glass through alcohol washing: a preliminary study. Biomatter 3(2):1–10. https://doi.org/10.4161/biom.24288

Qian J, Kang Y, Wei Z, Zhang W (2009) Fabrication and characterization of biomorphic 45S5 bioglass scaffold from sugarcane. Mater Sci Eng C Mater Biol Appl 29(4):1361–1364. https://doi.org/10.1016/j.msec.2008.11.004

Ramlee SNL, Sharifulden NSAN, Mohamad H, Noor SNFM (2019) Sol-gel derived bioactive glass scaffolds incorporated with polyvinyl-alcohol and pluronic P123 polymers using sponge replication technique. Mater Today Proc 17:966–975. https://doi.org/10.1016/j.matpr.2019.06.463

Rezaeipour Y, Alizadeh P, Keshavarz M (2023) Collagen scaff old impregnated with borosilicate bioactive glass for endometrial healing. Appl Mat Today

Rimpy, Ahuja M (2022) Fluconazole-loaded TEOS-modified nanocellulose 3D scaffolds—fabrication characterization and its application as vaginal drug delivery system. J Drug Deliv Sci Technol 75:103646. https://doi.org/10.1016/J.JDDST.2022.103646

Sarmast Sh M, George S, Dayang Radiah AB, Hoey D, Abdullah N, Kamarudin S (2022) Synthesis of bioactive glass using cellulose nano fibre template. J Mech Behav Biomed Mater 130:105174. https://doi.org/10.1016/j.jmbbm.2022.105174

Sarmast Sh M, Leow YS, Dayang Radiah AB, Abdullah N, Alijantabar Aghouzi S, Hoey DA, Kamarudin S, Zainuddin HS (2023) Evaluation of bioactivity and antibacterial properties of bioglass fabricated using a cellulose nano fibre template. Mater Chem Phys. https://doi.org/10.1016/J.MATCHEMPHYS.2023.127863

Scherrer P (1918) Bestimmung der Größeund der inneren Struktur von Kolloidteilchen mittels Röntgenstrahlen. Nachrichten von der Gesellschaft der Wissenschaften zu Göttingen, Mathematisch-Physikalische Klasse 1918: 98–100. http://eudml.org/doc/59018

Silva MJ, Alves W, Graeff CFDO, D'Alpino PHP (2021) Modified synthesis and physicochemical characterization of a bioglass-based composite for guided bone regeneration. Sci World J. https://doi.org/10.1155/2021/4295433

Sudhakar Y, Kuotsu K, Bandyopadhyay AK (2006) Buccal bioadhesive drug delivery — a promising option for orally less efficient drugs. J Control Release 114(1):15–40. https://doi.org/10.1016/J.JCONREL.2006.04.012

Sugumaran V, Pavithra AJ, Purushothaman B, Subramanian B (2024) Crucial chemical revelations in 45S5 bioactive glass via sequential precursor integration order. ACS Appl Bio Mater 7:1600–1620. https://doi.org/10.1021/acsabm.3c01099

Szczodra A, Tainio JM, Houaoui A, Liu H, Pohjola J, Miettinen S, Brauer DS, Massera J (2023) Impact of borosilicate bioactive glass scaffold processing and reactivity on in-vitro dissolution properties. Mater Today Commun 35:105984. https://doi.org/10.1016/J.MTCOMM.2023.105984

Wajda A, Sitarz M (2018) Structural and microstructural comparison of bioactive melt-derived and gel-derived glasses from CaO-SiO_2 binary system. Ceram Int 44(8):8856–8863. https://doi.org/10.1016/j.ceramint.2018.02.070

Wang Z, Gao T, Cui L, Wang Y, Zhang P, Chen X (2016) Improved cellular infiltration into 3D interconnected microchannel scaffolds formed by using melt-spun sacrificial microfibers. RSC Adv 6(3):2131–2134. https://doi.org/10.1039/C5RA25142G

Wu SC, Hsu HC, Hsiao SH, Ho WF (2009) Preparation of porous 45S5 Bioglass®-derived glass–ceramic scaffolds by using rice husk as a porogen additive. J Mat Sci Mat Med 20(6):1229–1236. https://doi.org/10.1007/s10856-009-3690-8

Wu Ch, Fan W, Gelinsky M, Xiao Y, Simon P, Schulze R, Doert T, Luo Y, Cuniberti G (2011) Bioactive SrO–SiO2 glass with well ordered mesopores: Characterization, physiochemistry and biological properties. Acta Biomat 7(4):1797–1806. https://doi.org/10.1016/j.actbio.2010.12.018

Xiao J, Wei Q, Xue J, Yang Z, Deng Z, Zhao F (2022) Preparation and in vitro bioactivity study of a novel hollow mesoporous bioactive glass nanofiber scaffold. Molecules. https://doi.org/10.3390/molecules27227973

Yadav C, Maji PK (2019) Synergistic effect of cellulose nanofibres and bio- extracts for fabricating high strength sodium alginate based composite bio-sponges with antibacterial properties. Carbohydr Polym 203(2018):396–408. https://doi.org/10.1016/j.carbpol.2018.09.050

Zamani D, Moztarzadeh F, Bizari D (2019) Alginate-bioactive glass containing Zn and Mg composite scaffolds for bone tissue engineering. Int J Biol Macromol 137:1256–1267. https://doi.org/10.1016/j.ijbiomac.2019.06.182

Zeitler TR, Cormack AN (2006) Interaction of water with bioactive glass surfaces. J Cryst Growth 294(1):96–102. https://doi.org/10.1016/j.jcrysgro.2006.05.029